Curvature-processing network in macaque visual cortex

Xiaomin Yue[a,1], Irene S. Pourladian[a], Roger B. H. Tootell[a,b], and Leslie G. Ungerleider[a,1]

[a]Laboratory of Brain and Cognition, National Institute of Mental Health, National Institutes of Health, Bethesda, MD 20892; and [b]Martinos Center for Biomedical Imaging, Massachusetts General Hospital, Charlestown, MA 02129

Contributed by Leslie G. Ungerleider, July 7, 2014 (sent for review March 12, 2014)

Our visual environment abounds with curved features. Thus, the goal of understanding visual processing should include the processing of curved features. Using functional magnetic resonance imaging in behaving monkeys, we demonstrated a network of cortical areas selective for the processing of curved features. This network includes three distinct hierarchically organized regions within the ventral visual pathway: a posterior curvature-biased patch (PCP) located in the near-foveal representation of dorsal V4, a middle curvature-biased patch (MCP) located on the ventral lip of the posterior superior temporal sulcus (STS) in area TEO, and an anterior curvature-biased patch (ACP) located just below the STS in anterior area TE. Our results further indicate that the processing of curvature becomes increasingly complex from PCP to ACP. The proximity of the curvature-processing network to the well-known face-processing network suggests a possible functional link between them.

curvature patches | face patches | curved Gabor filters

Decades of research have focused on understanding visual feature processing, particularly along the ventral visual pathway. Such studies have shown that neurons in lower-order visual areas (e.g., V1) respond strongly to simple oriented contours (1), whereas neurons in higher-order visual areas (e.g., inferior temporal cortex) respond selectively to more complex image features and/or visual categories (2–4), in ways that are not yet fully understood. To link these extremes in visual information processing, many studies have aimed to clarify the optimal "trigger" features at intermediate levels of the visual cortical hierarchy.

Among these features, stimulus curvature has not been well studied. This is surprising because, strictly, all lines are curved to some extent, except for the single exception of a perfectly straight line. This ubiquity of curved shapes also extends to 3D surfaces (5). In nature, where much of our visual system presumably evolved, perfectly flat surfaces are rare. Even the flattest of natural features (e.g., oceans, sandy beaches) are often curved to some extent, due to wind, water motion, and even the curvature of the earth. Thus, it is important to understand curvature processing to fully unravel the steps in cortical visual processing.

Among the few studies to test single neuron responses to curvature per se, Gallant et al. (6, 7) reported that a significant percentage of neurons in macaque cortical area V4 is selective for curved stimuli. Intriguingly, these authors also noted that neurons preferring curved patterns were often anatomically clustered together. Subsequently, Pasupathy and Connor (8–10) demonstrated that neurons in the parafoveal representation of dorsal V4 respond robustly to the curvature component of complex shapes. To our knowledge, there have been no systematic studies of curvature at levels below V4 in macaques.

Intriguingly, some evidence suggests that the processing of curvature may interact selectively with the processing of faces. For instance, perceptual deficits in face recognition (prosopagnosia) are sometimes associated with deficits in curvature discrimination (11). In addition, some neurons in face-selective regions of the temporal lobe also respond to rounded nonface objects (12, 13). A human functional magnetic resonance imaging (fMRI) study (14) reported that a concentrically curved grating produced a larger response in the fusiform face-selective area (FFA) (15, 16), compared with an otherwise identical linear grating.

Here, we tested for a cortical specialization of curvature processing, using fMRI in fixating macaque monkeys. Given the previous single-unit studies (6–10), we expected that curved stimulus features would activate V4, either in specific patches or distributed throughout the area. The present fMRI approach also allowed us to test whether curvature processing is confined to V4, or whether it extends into additional brain regions. If specialized areas for curvature processing were identified, we could then ask whether they might be topographically linked with face-selective regions. Such an arrangement would shorten the mean axonal length between curvature- and face-processing regions, if these regions were functionally related.

Results

Using fMRI, we tested curvature selectivity in the cortex of three male macaques. An exogenous contrast agent was injected i.v. to enhance the signal-to-noise ratio and functional selectivity. Six conditions were tested in a blocked design, including (*i*) round and (*ii*) rectilinear objects, and arrays of (*iii*) spheres and (*iv*) four-sided pyramids, plus images of (*v*) faces and (*vi*) objects. Our results showed that (*i*) stimulus curvature is processed selectively in discrete cortical patches, and (*ii*) some of these curvature patches are topographically related to the face-selective patches.

Significance

The brain processes visual stimuli along different feature dimensions, including edge orientation, visual motion, and color. To expedite visual processing, cells that process a common visual dimension are often anatomically grouped in cortical columns, patches, and/or areas. Here, we tested the hypothesis that (*i*) image curvature is one of these fundamental visual dimensions and, as such, (*ii*) curvature-selective cells are grouped together in discrete cortical areas. Using neuroimaging techniques, we confirmed this hypothesis and localized the curvature-processing sites in extrastriate visual cortex. These sites lay along a common cortical strip, spanning lower- to higher-level processing stages. Furthermore, the curvature-processing sites are adjacent to the well-known face-processing cortical areas, suggesting a possible functional link between them.

Author contributions: X.Y., R.B.H.T., and L.G.U. designed research; X.Y. and I.S.P. performed research; X.Y. analyzed data; and X.Y., R.B.H.T., and L.G.U. wrote the paper.

The authors declare no conflict of interest.

Freely available online through the PNAS open access option.

[1]To whom correspondence may be addressed. Email: yuex@mail.nih.gov or ungerlel@mail.nih.gov.

This article contains supporting information online at www.pnas.org/lookup/suppl/doi:10.1073/pnas.1412616111/-/DCSupplemental.

Experiment 1: Curvature Maps. We tested two different types of curved and rectilinear stimuli: (*i*) natural objects, and (*ii*) computer-generated shapes (Fig. 1 *A* and *B*). First, we found that both types of curved stimuli (Fig. 1 *A* and *B*) produced significantly greater activation in discrete cortical patches, compared with the rectilinear shaped stimuli. These two types of curvature-biased patches had an essentially equivalent localization in response to both the real-world objects and the computer-generated shapes (Fig. 2 *A* and *B*), thus supporting our interpretation that stimulus curvature was the common feature linking these two stimulus sets. Because of this similarity, data produced by those two contrasts were combined to more generally define the curvature-biased regions [i.e., (curved real-world objects plus computer-generated spheres) vs. (rectilinear real-world objects plus computer-generated pyramids); i.e., conditions *i* and *iii* vs. conditions *ii* and *iv*].

Despite minor variation in the topography across hemispheres and across animals, two robust, bilateral, curvature-biased patches could be identified in all six hemispheres, in both the individual maps (Fig. 3) and the group-averaged maps (Figs. 2 *A* and *B* and 4*A*). The most posterior curvature patch (PCP) was located in the near-foveal representation of dorsal V4 (17), on the prelunate gyrus, dorsal to the anterior terminus of the inferior occipital sulcus. A second patch, the middle curvature patch (MCP), was centered on average 3.1 cm anterior-ventral to PCP, near the ventral lip of the posterior superior temporal sulcus (STS), and 2.1 cm dorsal to the posterior terminus of the posterior middle temporal sulcus (PMTS), most likely within architectonic area TEO. In addition, a small patch of weaker curvature-biased activity [anterior curvature-biased patch (ACP)] was found more anteriorly in four of the six hemispheres, located near the anterior tip of the temporal lobe just below the STS in architectonic area TE (Fig. 4*A*). This small patch of weaker activity survived the group averaging for the left but not the right hemisphere. No other cortical regions showed consistent curvature-biased patches. However, at lower thresholds, additional visual cortical regions showed a bias for curvature, relative to that for the rectilinear stimuli (Fig. S1).

Topographic Relationship of Face- and Curvature-Processing Regions. To study the relationship between these curvature-biased patches and the well-known face-selective patches, we localized the latter by contrasting activity produced by faces (condition *v*) vs. (nonshape specific) objects (condition *vi*), in all three monkeys (Fig. 1*C*).

As expected from prior studies (12, 18–21), this contrast revealed a strongly activated patch extending from the fundus of STS onto the dorsal inferior temporal gyrus within area TEO, in all six hemispheres. This main patch of face-selective activity has been called the "posterior" (19, 20) or "middle" (12) face patch in prior studies (Fig. 4*B*); here, we refer to it as the posterior face patch (PFP). The contrast of faces vs. objects also localized a weakly activated patch within anterior area TE, located dorsally on the inferior temporal gyrus just below the ventral lip of the STS, which we (19–21) and others (12, 13, 18) refer to as the anterior face patch (AFP) (Fig. 4*B*).

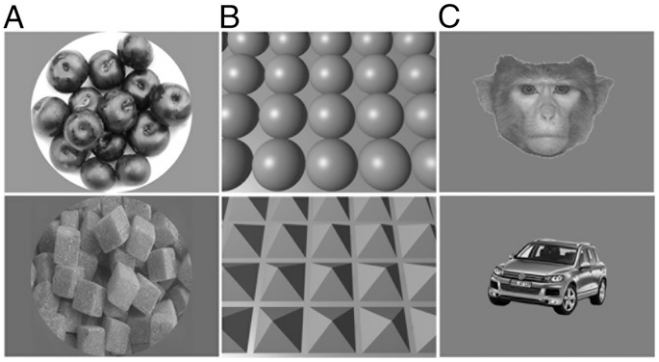

Fig. 1. Examples of stimuli used in experiment 1. (*A*) Real-world round vs. rectilinear shapes; (*B*) computer-generated 3D spheres vs. pyramid arrays; (*C*) faces vs. objects.

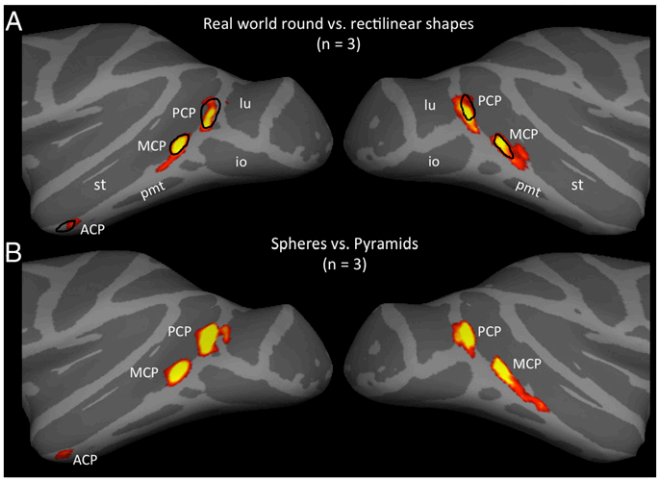

Fig. 2. Convergent curvature-biased cortical regions revealed by the two types of stimuli. The group averaged contrast map of (*A*) real-world round (red-yellow) vs. rectilinear shapes and (*B*) computer-generated 3D sphere (red-yellow) vs. pyramid arrays ($n = 3$). The locations of the curvature patches are almost identical in *A* and *B* (for comparison, regions in yellow in *B* are shown as black lines in *A*). The uncorrected statistical threshold is $P < 10^{-17}$ (red) for *A* (Bonferroni corrected: $P < 10^{-12}$), and $P < 10^{-6}$ (red) for *B* (Bonferroni corrected: $P < 0.05$). The capitalized letters label the curvature-biased patches: ACP, anterior curvature patch; MCP, middle curvature patch; PCP, posterior curvature patch. Major sulci are labeled in lowercase letters: io, inferior occipital sulcus; lu, lunate sulcus; pmt, posterior middle temporal sulcus; st, superior temporal sulcus.

Our results showed that MCP was located dorsal-posterior to PFP (Fig. 4*A*). In the group-averaged map, the center-to-center distance between the activity peaks of MCP and PFP was 2.2 cm. Both sets of group-averaged patches were elongated and collinear, and located immediately adjacent to each other at the thresholds used here (uncorrected: $P < 10^{-17}$ for MCP, and $P < 10^{-6}$ for PFP; Bonferroni corrected: $P < 10^{-12}$ for MCP, and $P < 0.05$ for PFP). By contrast, in the corresponding group-averaged map of the left hemisphere, the center of ACP was very close to the center of AFP (<4 mm).

Fig. 4*C* illustrates the location of the group-averaged curvature patches relative to the borders of well-known neighboring visual cortical areas. Those areal borders were based on standard retinotopic and motion-selective localizing stimuli (*Methods*). Based on the results, PCP was located ~4 mm posterior to MT on the cortical surface (lateral to MT in vivo), within the fovea representation of V4d. MCP was located on the ventral lip of STS, anterior and lateral to MT.

Curvature-Biased Patches: Quantitative Measures of Image Curvature. To clarify the functional responses in the curvature-biased patches, we defined regions of interest (ROIs) in all three patches, in each of the three animals, using the functional contrast of (curved real-world objects plus computer-generated spheres) vs. (rectilinear real-world objects plus computer-generated pyramids). The subsequent data analysis was based on these ROIs.

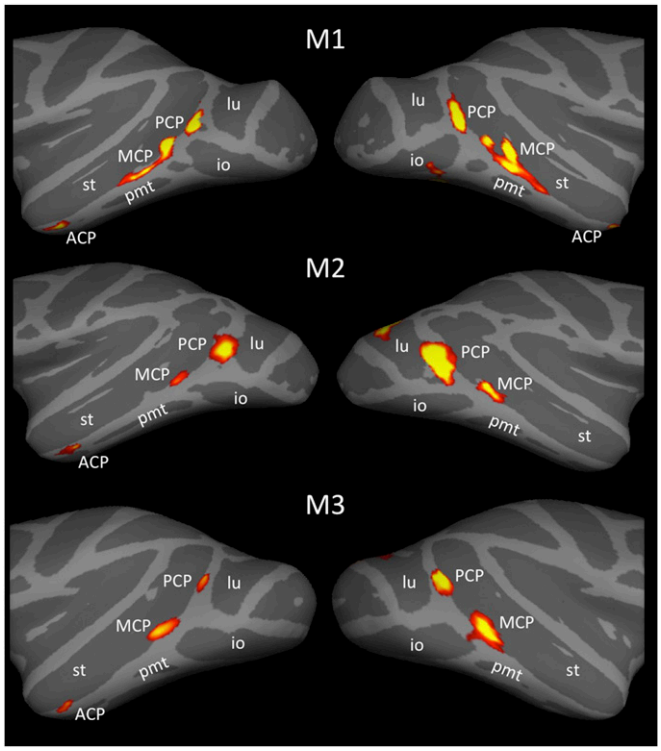

Fig. 3. Curvature-biased patches in each of the three animals tested. The maps were generated by contrasting responses to round (real-world and sphere array) vs. rectilinear (real-world and pyramid array) stimuli. The uncorrected statistical threshold is $P < 10^{-9}$ (red) for M1, M2 (Bonferroni corrected: $P < 10^{-4}$), and $P < 10^{-6}$ (red) for M3 (Bonferroni corrected: $P < 0.05$). Two bilateral curvature-biased peaks of activity (curvature "patches") were identified across all six hemispheres. Based on the cortical topography, the posterior curvature patches (PCPs) were located in the near-foveal representation of dorsal V4, on the prelunate gyrus, dorsal to the anterior terminus of the inferior occipital sulcus. The middle curvature patches (MCPs) were located near the ventral lip of the posterior STS within architectonic area TEO. The third curvature patches (ACPs) were small and low in amplitude, observed in four of the six hemispheres, located near the anterior tip of the temporal lobe just below the STS in architectonic area TE. For abbreviations, see Fig. 2.

In PCP, the group-averaged responses correlated significantly with the curved Gabor filter values (*Methods*) (Fig. 5*A*) ($r = 0.79$, $P < 0.05$, one tail). By contrast, the fMRI activity did not correlate significantly with values of the Gabor filters (for PCP, $r = 0.62$, $P > 0.1$, one tail; for MCP, $r = 0.39$, $P > 0.1$, one tail; for ACP, $r = 0.05$, $P > 0.1$, one tail), in any of these patches. These results support the interpretation that PCP is involved in processing simple curvature. The results are also consistent with previous reports of curvature processing by single V4d neurons (6–10, 22, 23).

The correlation between fMRI amplitude and the curved Gabor filter values was not significant in MCP ($r = 0.58$, $P > 0.1$, one tail) (Fig. 5*B*) or ACP ($r = 0.25$, $P > 0.1$, one tail) (Fig. 5*C*). However, further analysis showed that a weighted linear combination of simple curvature (*Methods*) could significantly account for the fMRI responses in MCP ($r = 0.82$, $P < 0.05$, permutation test) (Fig. 6*A*), but not in ACP ($r = -0.21$, $P > 0.1$, permutation test) (Fig. 6*B*). Together, these results suggest that (*i*) complex features derived from simple curvature may be processed in MCP, and (*ii*) bottom-up input to MCP might arise from PCP, at least in part.

Such a general increase in the complexity of stimulus selectivity, from posterior to anterior along the ventral stream, is consistent with many previous single-unit studies (e.g., refs. 10 and 24–27). To test this idea further in our fMRI data, we defined a curvature selectivity index as the difference in fMRI activity between the curved and rectilinear conditions, divided by the sum of these conditions. Fig. 6*C* confirmed that this index increased significantly from the posterior to anterior curvature patches [$F_{(1,2)} = 56.15$; $P < 0.05$].

Experiment 2: Testing for Retinotopy of Curvature Patches. Based on its cortical location, PCP appeared to be located in dorsal V4. If so, it should be activated selectively by stimuli in the contralateral lower visual field. To test this, we performed an additional experiment in which simple curvatures (Fig. S2) were presented in each of the four visual field quadrants, at 5° eccentricity. The curvature-biased ROIs for the three monkeys were defined independently from the results of experiment 1, by contrasting (curved real-world objects plus computer-generated spheres) vs. (rectilinear real-world objects plus computer-generated pyramids). As shown in Fig. 7, the main curvature patches (PCP and MCP) showed a significant activity bias for stimuli in the contralateral visual field [for PCP; $F_{(1,2)} = 22.95$, $P < 0.05$; for MCP,

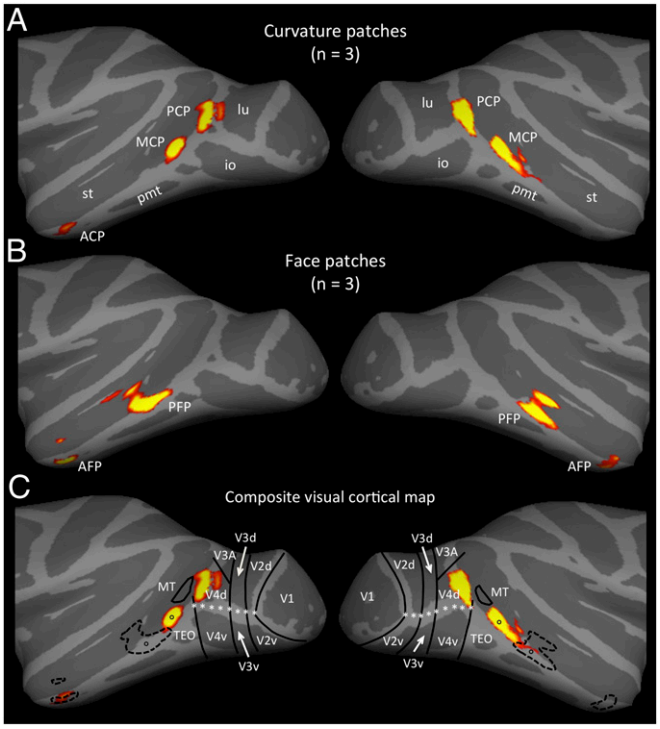

Fig. 4. Location of the curvature-biased patches and face-biased patches in the group-averaged data ($n = 3$), along with the areal borders of neighboring retinotopic and motion-selective areas. Two curvature patches (PCP, MCP) were identified in both hemispheres (*A*). The anterior curvature patch (ACP) was identified in the left hemisphere only. In the same group of animals, two face patches were evident in both hemispheres (*B*). Based on previous studies, these were identified as the posterior face patch (PFP) and the anterior face patch (AFP) (19–21). *C* illustrates the retinotopic and MT borders superimposed on the curvature-biased map (*A*). The location of these face patches (*B*) is shown in *C*, outlined in black dotted lines. The line of asterisks indicates the representation of the fovea. The peaks of MCP is located posterior to PFP, 2.2 cm apart (peak to peak), are indicated using black circles. The degree of overlap between ACP and AFP is dependent on the statistical threshold, but the peak locations are not; the peak of ACP is 0.37 cm away from the peak of AFP. The uncorrected statistical threshold in the activity map is $P < 10^{-17}$ for *A* (Bonferroni corrected: $P < 10^{-12}$), and $P < 10^{-6}$ for *B* (Bonferroni corrected: $P < 0.05$). Variations in the statistical threshold do not change the peak location of the patches.

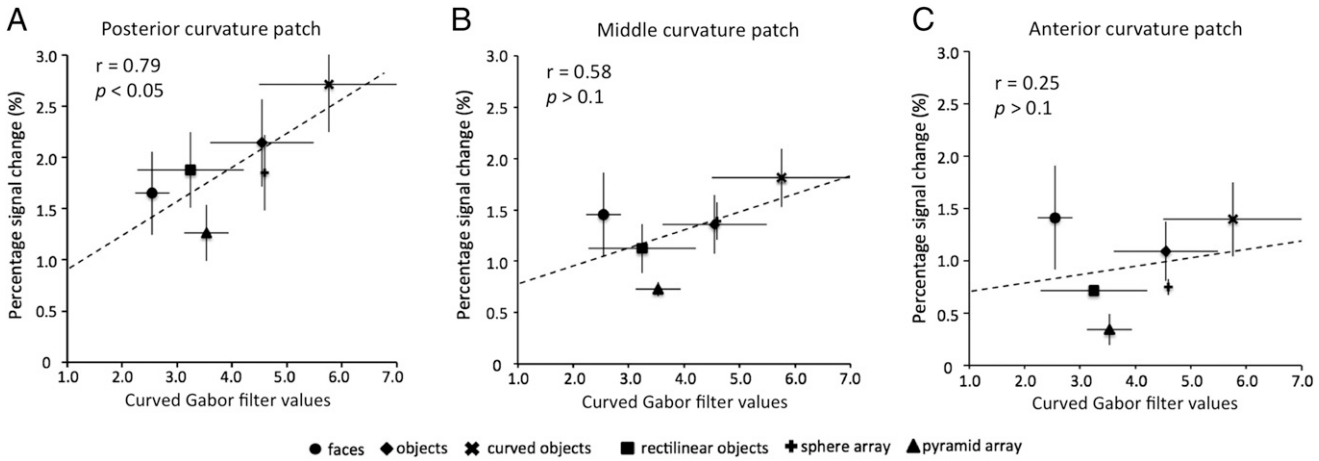

Fig. 5. Correlations of curved Gabor filter values and fMRI activity in the curvature-biased patches. The *x* axis represents the curved Gabor filter values, and the *y* axis represents the fMRI activity. The correlation is significant in PCP (*A*), but not in MCP (*B*), or ACP (*C*). This suggests that PCP is involved in processing simple curvatures. The error bars represent SEM.

$F_{(1,2)} = 1752.51$, $P < 0.01$], consistent with the well-known crossed representation of the visual field in cortex (28–30). In PCP, the activity was also strongly biased for stimuli in the lower visual field ($t_{(2)} = 4.97$; $P < 0.05$), which supports the conclusion that this patch is located in dorsal V4. However, in MCP, we found no significant difference between activation evoked by stimuli in the upper vs. lower visual field [$F_{(1,2)} = 0.01$; $P > 0.1$]. ACP showed no bias for stimuli in the contralateral visual field [$F_{(1,2)} = 1.41$; $P > 0.1$] or for those in the upper or lower visual field [$F_{(1,2)} = 0.39$; $P > 0.1$]. These retinotopic fMRI results are consistent with previous electrophysiological mapping studies (31, 32) and suggest that MCP is located in TEO and ACP is in TE.

Regions Biased for Rectilinear Stimuli. Given this evidence for a cortical segregation of curvature processing, one might ask whether a complementary segregation exists for the processing of noncurved (straight) lines and/or flat surfaces, which would be reflected in significantly greater activation by the rectilinear stimuli used here. In one respect, this hypothesis was not confirmed: at the relatively stringent thresholds ($P < 10^{-17}$, uncorrected) shown in Figs. 2 and 4*A*, activity biases were present only for the curved stimuli, and not for the rectilinear stimuli. However, lower thresholds ($P < 0.01$, uncorrected) revealed a set of patches that were activated more by the rectilinear than the curved stimuli (Fig. 8). Importantly, the location of these rectilinear-biased patches was consistent across both hemispheres in the group-averaged map. One pair of patches was located immediately adjacent to the foveal representation in areas V1 and V2 (white asterisks in Fig. 8), likely reflecting a near-foveal interaction of the fixation target with differences in the background stimuli. Two other rectilinear-biased patches were located farther anteriorly, and bilaterally: (*i*) in/near V3A and (*ii*) near the posterior middle temporal sulcus. These latter two locations are in/near the locations of scene-responsive patches of activity in macaques (ref. 33; see also ref. 34), which are thought to be homologous to scene-selective sites in humans, namely, (*i*) the transverse occipital area (TOS) and (*ii*) the parahippocampal place area (PPA) (35), respectively. In human subjects, rectilinear objects and shapes also preferentially activate these scene-selective areas (36–38). However, as scene-selective areas were not localized in our monkeys, this idea could not be directly tested.

Discussion

A Cortical Architecture for Curvature Processing. By comparing the fMRI activity produced by curved vs. rectilinear shapes, we found three patches of cortical activity that showed a significant bias for curved (relative to rectilinear) stimuli. One of these patches was located on the prelunate gyrus, and another was located on the ventral bank of the posterior STS. A third patch, much smaller and lower in amplitude than the others, was located just below the ventral lip of the anterior STS, in four of the six hemispheres tested, at a threshold of $P < 10^{-6}$. To our knowledge, this is the first neuroimaging evidence for a cortical network of curvature processing in macaque visual cortex.

Throughout visual cortex, cortical columns and patches reflect an important organization for the selective processing of visual features. Familiar examples include the ocular dominance (39, 40) and orientation columns in V1 (41), orientation- and color-segregated columnar stripes in V2 (42, 43), columns for direction of motion in MT/V5 (44), and subregions for object-related properties and face selectivity in the inferior temporal (IT) cortex (12, 27, 45). Presumably, columns/patches arise because such an architecture allows shorter axonal connections between neurons that require a great deal of interaction—i.e., functionally similar neurons. Thus, the current evidence for curvature-selective patches in V4 suggests that curvature processing becomes explicit in that area, perhaps for the first time along the visual cortical hierarchy. For one thing, the larger receptive field diameter in V4 (relative to V1 or V2) furnishes a larger surface area within which a given radius of curvature can be calculated.

Another possibility is that curvature-selective columns/patches do exist within visual cortical areas before V4, but that this organization cannot be spatially resolved using fMRI. For instance, it can be imagined that curvature-selective cells are systematically mapped within each orientation column in V1 or V2, but that this organization is below the spatial resolution of the fMRI. However, the monocrystalline iron oxide nanocolloid (MION)-based imaging and relatively small voxels (1.5 mm^3) used in the present study would argue against this possibility. Both these scanning factors improve on known limitations with conventional blood oxygen level-dependent imaging in humans, although perhaps not adequately to resolve a hypothetical curvature organization in early visual areas. Given the dearth of single-unit data on curvature tuning in V1, V2, and V3, one can only speculate on possible precursors to V4 in curvature tuning.

The strong retinotopic bias for stimuli in the contralateral lower visual field (Fig. 7) confirmed that PCP is located in dorsal

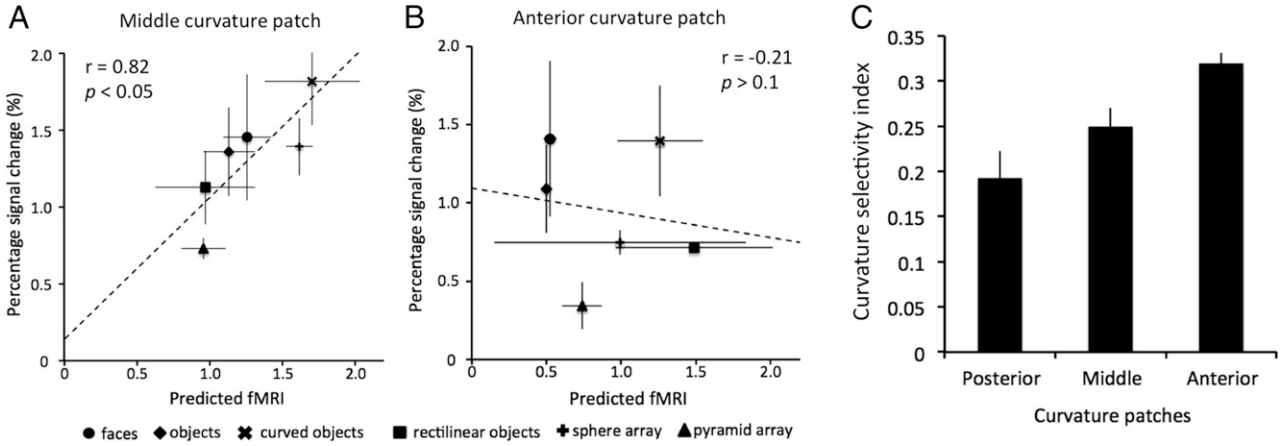

Fig. 6. Correlation of the predicted response from the linear combination of curved Gabor filter values with fMRI activity in MCP and ACP, and the curvature selectivity index in the curvature-biased patches. The curvature selectivity index (*C*) is defined as the fMRI activity difference between the curved and rectilinear conditions, divided by the sum of these conditions. The correlation is significant in MCP (*A*), but not in ACP (*B*), suggesting that MCP is involved in processing complex features derived from simple curvatures. The curvature selectivity index (*C*) increased significantly from PCP to ACP [$F_{(1,2)} = 56.15$; $P < 0.05$].

V4. Because that curvature patch was located in dorsal V4, one might expect to find a counterpart curvature patch located in ventral V4, i.e., selectively responsive to stimuli in the contralateral upper visual field. However, our fMRI tests did not confirm such a hypothetical curvature patch in ventral V4. However, dorsal-ventral asymmetries have been reported in V4d/V4v, based on both electrophysiology (17) and fMRI maps (46, 47). Thus, it is possible that this dorsal-ventral asymmetry is simply reflected in our fMRI results. Alternatively, the apparent absence of a distinguishable curvature-biased patch in ventral V4 might be due to signal drop-off in this cortical region, which has been reported in previous studies (48, 49).

Conventional tracer studies (e.g., ref. 50) have demonstrated strong feedforward projections from V4 to TEO. To the extent that MCP is located within TEO, one might expect that some outputs of PCP project directly to MCP. In turn, this raises the possibility that simple curvature information evident in PCP is pooled and computed into more complex curvature coding within MCP. Such pooling of information is consistent with the increase in receptive field size from V4 (17, 51) to TEO (31, 52). Our linear weighting analysis (Fig. 6*A*) further supports the idea that MCP receives inputs from PCP, and combines those inputs to generate a more complex curvature coding. However, if the dominant inputs to MCP were from PCP, then MCP, like PCP, would have a lower visual field bias, which was not observed in our retinotopic data.

As shown in Fig. 4*C*, we also found that MCP is located adjacent to MT in the cortical map. This raises the possibility that curvature information is transmitted between MCP and MT, perhaps to help interpret moving curved stimuli. Such curved information could help distinguish motion direction compared with analysis based on noncurved stimuli. For instance, curved edges do not produce the direction ambiguity that is produced by straight edges in the "barber shop illusion" (53).

ACP showed a negligible response to simple curved features (Fig. 7*C*), but it also showed the largest curvature selectivity index (Fig. 6*C*). Are those two pieces of evidence contradictory? We think not. First, our analysis of curved Gabor filters suggests that ACP processes neither simple curvature nor the linear combination of simple curvatures; therefore, it was not surprising

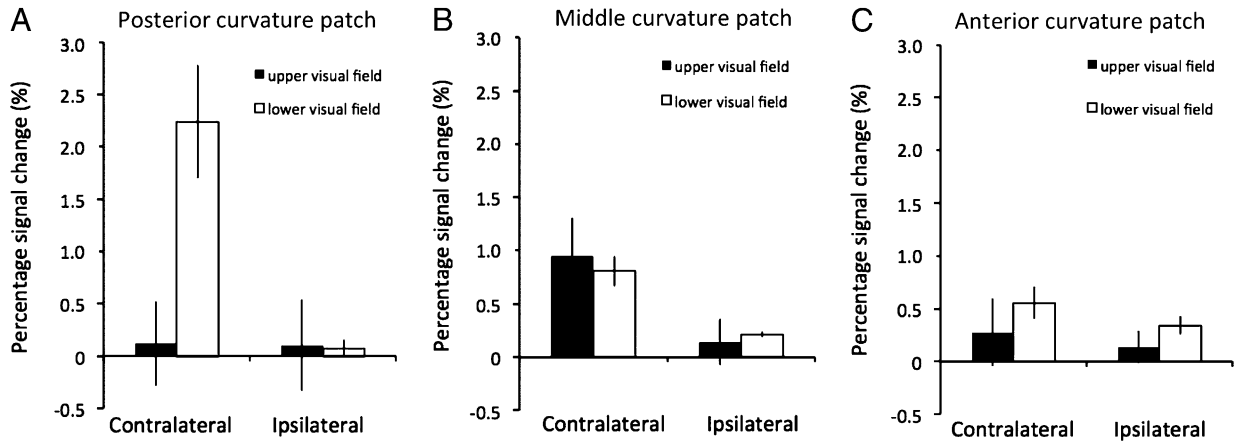

Fig. 7. Results of experiment 2. Responses in PCP (*A*) were significantly biased to stimuli presented in the contralateral lower visual field [$t_{(2)} = 4.97$; $P < 0.05$]. MCP (*B*) had a significantly larger response to stimuli presented in the contralateral relative to the ipsilateral visual field [$F_{(1,2)} = 1{,}752.51$; $P < 0.01$], but showed no difference between the upper and lower visual fields. ACP (*C*) showed a very weak response to the simple curvatures used in these stimuli, without a significant preference for any visual field quadrant.

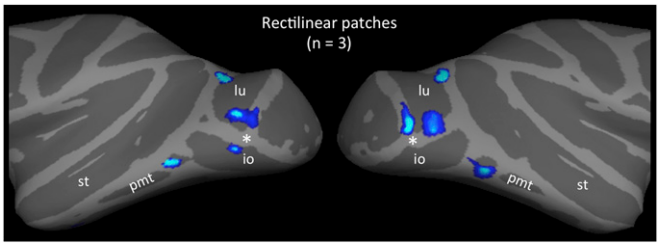

Fig. 8. Preferential response to rectilinear stimuli. In the locations rendered in blue-cyan, the group averaged map showed a larger response to rectilinear stimuli than curved stimuli. The statistical threshold is $P < 10^{-2.5}$ (Bonferroni corrected: $P > 0.1$). The asterisk indicates the foveal representation of the visual field at the V1/V2 border. Two additional rectilinear-biased patches were located more anteriorly, one dorsally in/near V3A, and the other ventrally near the posterior middle temporal sulcus (pmt).

that ACP was significantly less activated by the simple curvatures used in experiment 2. Second, the large curvature selectivity index in ACP (compared with MCP) was produced by larger decreased activity to rectilinear shapes compared with round shapes in ACP (Fig. 5). This finding suggests that ACP may process the subset of curved shapes having few or no rectilinear components.

Relationship Between Curvature and Face Processing. One intriguing aspect of the current results was the close topographical relationship between the curvature patches and the well-known face patches in the cortical maps. This close topographical relationship suggests a functional link between these two processing streams, because such adjacency minimizes axonal length between cells that process highly related information.

Perhaps the largest and most strongly activated of both types of patches were the MCP and the PFP. At thresholds from a range that is common for fixed-effect MION imaging in monkeys ($P < 10^{-17}$ for MCP and $P < 10^{-6}$ for PFP), these two patches (curvature and face) were found to be elongated and collinear, sharing a common boundary between them. At lower thresholds, these curvature-defined and face-defined patches overlapped. In these topographical respects, these face and curvature patches appear to be related.

However, the presence of cortical adjacency alone does not guarantee that such adjacent areas share strong connections, or similar functional properties (as in a comparison of V4d and MT). Moreover, the peaks of MCP and PFP were separated by more than 2 cm, when measured across the cortical surface—a significant distance in macaque visual cortex. A simple interpretation is to assume an extended functional transition from lower-level curvature sensitivity to more specific face selectivity, along a single cortical strip, from V4d through TEO, respectively.

Near the anterior pole of the temporal lobe, in higher tier area TE, we found an additional pairing of curvature and face patches (namely, ACP and AFP). Here, both patches were quite small and less strongly activated across animals, although both patches were somewhat elongated and parallel to the ventral lip of the anterior STS—the same axis of elongation as that described above. The "anterior face patch" is well described previously (54, 55); the previously unidentified finding here is that a partially overlapping patch was also activated in the test for curvature. These data suggest that the topographically segregated mapping of information (from curved- to face-selective) in more posterior cortex (described above) converges to some extent in anterior temporal cortex, at least in the fMRI maps.

As described above, we also found a strongly activated curvature patch (PCP) at a quite early stage in the cortical hierarchy. This patch was located in V4d, based on the known location of V4 on the prelunate gyrus, and confirmed by a lower visual field bias found in our fMRI retinotopic mapping. However, unlike the other curvature patches, we found no face patch in the vicinity of the V4d curvature patch. Although a "posterior" face patch has been reported by other groups (54), that face patch was instead reported in/near the near-foveal representation of ventral V2/V3, i.e., not near our PCP. Thus, overall, our data suggest that curvature is first extracted (or first made explicit in the fMRI) in PCP, and is progressively aligned and then merged with face information at more anterior (i.e., higher tier) processing stages.

Relationship to Previous Physiological Evidence. Our finding of a curvature-biased patch in V4 (PCP; Figs. 2 and 3) is generally consistent with previous electrophysiological findings (6–10, 22, 23). The nature of the curvature selectivity tested in previous reports was simple enough so that, presumably, it could be evident in results from our curved Gabor filter analysis (Fig. 5). A more recent single-unit study (22) directly confirmed that V4 neural responses can be well modeled by curved Gabor filters, similar to what we used in our analysis here.

A different study (25) recorded neuronal responses to complex shapes in TEO and/or posterior TE, where we found MCP to be located. These stimuli were 2D line drawings composed of straight lines and curved components. When presented independently, each of those components produced distinctive neuronal activity. When the component shapes were presented as a whole, the neuronal activity was accurately modeled by the summation of activity evoked by each component. Although it is difficult to generalize neural recording results to fMRI, that single-unit result is consistent with the idea that MCP processes more complex curvature features derived from the linear combination of simple curvature features, processed in PCP.

Two additional studies (56, 57) showed that single-unit activity recorded from anterior IT cortex includes information necessary to distinguish curved vs. straight nonfamiliar irregular shapes, at both the individual and population levels. It is possible that their recording sites were located within/near ACP.

Previous fMRI Studies. In previous fMRI studies, including those in awake monkeys, the anterior portion of IT cortex was reported to show stronger activity in response to smoothly curved computer-generated 3D shapes ("smoothies"), compared with more angular shapes ("spikies") (58, 59). Moreover, this curvature-biased region partially overlapped the anterior temporal face patch, as measured by an fMRI face localizer. Although those data are not inconsistent with the current data in anterior temporal cortex, several differences limit a direct comparison. First, those studies (58, 59) did not specifically test the effects of curved vs. rectilinear stimuli; instead the tested stimuli included multiple shapes in addition to simple curvature and right angles. Second, the previous studies did not find our strongest curvature patches, namely, those located in V4d and posterior STS. However, they found (as did we) overlap between an anterior temporal curvature-biased region and the anterior temporal face patch.

In human subjects, one study (14) reported higher responses in V4 to concentric patterns, compared with parallel patterns. This result suggests a bias for curved stimuli, consistent with the current and previous results in macaque. However, the relationship between "dorsal V4" in humans and monkeys is controversial (60).

Using fMRI methods based on adaptation (61) or multivoxel pattern analysis (62), two studies have reported that the occipital face area (OFA) (63) (a more posterior region involved in face processing in the human brain) encodes the external head outline (e.g., an oval shape) more than whole faces, compared with the more anterior FFA. In such studies in human subjects, this general trend is consistent with the idea that curvature is

processed at posterior levels (e.g., OFA), and more holistic face processing at higher, more anterior levels (e.g., FFA). A similar functional trend is implied in our data with monkeys. However, as noted above, more research is needed to draw definitive parallels between corresponding areas in the two species.

Previous Psychophysical Studies. Psychophysical studies have demonstrated the importance of curvature in shape recognition (64, 65), suggesting that curvature may be encoded independent of other shape dimensions, including symmetry and aspect ratio. However, there is little neural evidence to support these psychophysical findings. Here, we provide evidence for cortical regions dedicated to curvature processing, which might ultimately clarify how and where those psychophysical observations (e.g., refs. 11 and 66–68) are instantiated in the brain.

Conclusion

Using awake monkey fMRI, we demonstrated a network of cortical areas selective for the processing of curved features along the ventral visual pathway. The network includes three patches: a posterior curvature-biased patch located in the near-foveal representation of dorsal V4 (PCP), a middle curvature-biased patch located in the posterior STS within TEO (MCP), and an anterior curvature-biased patch located in anterior TE just ventral to the STS (ACP). These three patches are organized hierarchically, with PCP processing simple curvature, MCP processing moderately complex curved features, and ACP processing shapes mainly composed of curved components. These results set the stage for future studies, which can clarify how those patches are anatomically linked, what the response properties of neurons within each of those patches are, and how this segregation contributes to object recognition. The proximity of the curvature-processing network to the well-known face-processing network implies a functional interaction between them, which should be clarified in further studies.

Methods

Subjects. Three male rhesus monkeys (5–8 kg) were used in experiments 1 and 2, based on scanning procedures described in previous publications (45). All experimental procedures were approved by the National Institute of Mental Health Animal Care and Use Committee.

Each monkey was implanted with a MRI-compatible plastic headset. After recovery, the monkeys were adapted to sit inside a plastic restraining chair, ultimately positioned within the scanner. Both in training and in the subsequent experiments, eye position was monitored using an infrared pupil tracking system (ISCAN) at 120 Hz. Monkeys were rewarded for maintaining fixation on a small (0.35° diameter) central target that was superimposed on all stimuli, to produce extended periods of central fixation.

Monkey Imaging. After fixation performance reached asymptote during training, we began functional scanning. Only scanning sessions with adequately high behavioral performance (>90% central fixation throughout the duration of each run) were analyzed further.

Before each scanning session, an exogenous contrast agent (MION; 14 mg/kg) was injected i.v. to enhance the signal-to-noise ratio and functional selectivity (69, 70). For ease of comparison, the polarity of the MION-based MR response was inverted for data analysis. The scan was conducted in a vertical 4.7-T scanner (Bruker), using an eight-channel surface coil. The echo planar imaging scan parameters were as follows: repetition time (TR), 2 s; echo time (TE), 14.29 ms; flip angle, 75°; 28 slices, in-plane matrix size, 64 × 34. Voxel size was 1.5 mm isotropic. In addition, seven anatomical scans were collected and averaged from each monkey, using a customized single-loop coil in a horizontal 4.7-T Bruker scanner (TR, 2.98 s; TE, 4.3 ms; flip angle, 12.9°; 0.5 mm isotropic; National Institutes of Health version of modified driven equilibrium fourier transform imaging). These anatomical data were used to create the cortical surfaces for each monkey using FreeSurfer (http://surfer.nmr.mgh.harvard.edu).

During the functional scanning, the monkeys sat inside a vertical MRI-compatible chair. The stimuli were projected onto a screen within the bore, via a LCD projector (Avotec; 1,024 × 768 pixels) using PsychToolbox (71, 72). Monkeys viewed stimuli via a mirror in front of their eyes. Eye gaze was monitored by an infrared pupil tracking system (ISCAN). Dynamic measurements of eye position were fed into a QNX-based eye tracking software program that controlled reward delivery based on the monkey's performance.

Experimental Design and Stimuli. Experiment 1 tested for the possible existence of a curvature-processing network. It included six conditions, four of which compared round (i.e., circular or spherical) vs. rectilinear stimuli. Rectilinear stimuli were chosen as a control for round stimuli because rectilinear stimuli lack curved contours and surfaces, but (like circles and spheres) they are also closed figures. The six conditions included (*i*) round and (*ii*) rectilinear objects, and arrays of (*iii*) spheres and (*iv*) four-sided pyramids, plus two conventional localizers: (*v*) faces and (*vi*) objects. The four-sided pyramids are essentially cubes, viewed from an atypical viewpoint and bisected by the common array plane. Complete image sets for conditions *i*, *ii*, *iii*, and *iv* are included in Fig. S3.

Face stimuli (condition *v*) were individual monkey faces, photographed from a colony independent from the one in which the tested monkeys were housed. Images of the stimulus objects were downloaded from the internet, including a wide range of common objects, both curved and rectilinear. All of the localizer stimuli (objects and faces) were initially unfamiliar to the monkey subjects. The original backgrounds of those faces and objects were removed digitally using Photoshop to generate isolated faces and objects. For each isolated face or object, retinal image size was equated based on surface area. On average, stimuli extended 14 × 12° of visual angle. The root mean square contrast of monkey faces and objects was also equated using customized Matlab codes (Fig. 1*C*) (73).

We used a block design, in which blocks were presented in semirandom order along with alternating baseline blocks of a uniform gray display. Eight images were presented for 1 s each, twice per block, in semirandom order. Each run lasted 3 min and 28 s. Each animal was scanned in four to six sessions, with 17–30 runs per session.

Experiment 2 examined the retinotopy of the regions within the curvature network observed in experiment 1. Experiment 2 included four conditions, corresponding to each of the four quadrants of the visual field. Our pilot study showed that the curvature-biased regions responded most strongly to acutely curved stimuli, compared with more obtuse (gradually) curved stimuli. Therefore, in each quadrant, acutely curved stimuli (radius, 3°) were presented with eight images of different orientations. These stimuli (Fig. S2) were generated using the curved Gabor filters described below with the largest curvature value allowed. The stimuli were centered 5° from the center of fixation. As in experiment 1, a block design was used in experiment 2. Each run included all four conditions and lasted 9 min and 4 s. Each animal was scanned in three sessions, with 16–25 runs per session.

fMRI Data Analysis. Each individual brain was inflated using FreeSurfer software (http://surfer.nmr.mgh.harvard.edu). Statistical analysis of the functional data was performed with the FreeSurfer Functional Analysis Stream (FS-FAST) (74). All functional images were preprocessed with motion correction, slice-timing correction, spatial smoothing (a 2-mm Gaussian kernel), and normalized across sessions individually. Following those preprocessing steps, the functional data were regressed with the general linear model (GLM), such that each condition was modeled as a convolution of a boxcar with a MION-based hemodynamic response function. To reduce the influence of body movement on the data analysis, the three motion measurements generated from the 3D motion correction were included in the GLM fitting, in addition to the experimental conditions.

Average signal intensity maps were calculated for each condition, for each subject. Voxel-by-voxel statistical tests were conducted by computing contrasts based on the β values derived from the GLM fitting described above. To generate a group-averaged map, all functional data were transformed into an individual monkey brain (in this case, M1) using a spherical transformation (75). Then, the GLM fitting was conducted on the transformed functional data.

The retinotopic borders were generated by extrapolating published data into the inflated monkey brain used in our study (17, 45, 76, 77). The MT borders were projected onto Fig. 4*C* from a single monkey's data in which MT was defined using a moving-vs.-stationary localizer.

Quantifying Image Curvature. Curved Gabor filters developed by Krüger and colleagues (78) were used to quantify the curvature in each image. The curved Gabor filters are a product of a rotated complex harmonic wave function and a 2D bent and rotated Gaussian. It is formulated as follows:

$$B^{\vec{b}}(x,y) = I^{\vec{b}} * G^{\vec{b}}(x,y) * \left(F^{\vec{b}}(x,y) - DC^{\vec{b}}\right),$$

where $F^{\vec{b}}$ is the rotated complex harmonic wave function, $G^{\vec{b}}$ is the 2D bent and rotated Gaussian, and a vector $\vec{b}$ includes three variables: frequency, orientation, and level of curvature. The bank of curved Gabor filters is composed of 120 individual curved Gabor filters, including three spatial scales, eight orientations, and five levels of curvature.

A stimulus image was convoluted with the bank of curved Gabor filters, which produced 120 ($3 \times 8 \times 5$) curved Gabor coefficients, each presented as an image. Each curved Gabor coefficient image, including complex and real components, represented the result from a curved Gabor filter with a unique combination of a scale, an orientation, and a level of curvature. The magnitudes of each curved Gabor coefficient image on each pixel were calculated as the square root of the sum of squared coefficients of complex and real components. The magnitudes were averaged spatially to generate a single curved Gabor filter value representing the amount of curvature captured by that parameterized curved Gabor filter. One hundred twenty curved Gabor filter values generated by repeating the above procedure for each of the 120 curved Gabor coefficient images were averaged to produce a curved Gabor filter value for the stimulus image.

For each condition, a curved Gabor filter value was produced by averaging all eight curved Gabor filter values of the eight images in each condition. This curved Gabor filter value represented the amount of curvature in that condition across scales, orientations, and levels of curvature.

Linear Combination of Simple Curvature. Using the procedure described above, the 120 curved Gabor filter values generated for each image were collapsed across three scales and eight orientations, while keeping the curvature dimension (five levels of curvature in the curved Gabor filters) intact. This yielded five curved Gabor filter values, each representing one level of curvature regardless of scale and orientation. Then, the five curved Gabor filter values were grouped into three curved Gabor filter values, as follows. The two curved Gabor filter values describing the smallest levels of curvature were averaged to yield a curved Gabor filter value representing a low level of curvature; the two filter values describing the largest levels of curvature were averaged to yield a curved Gabor filter value representing a high level of curvature. The curved Gabor filter value with the medium level of curvature was kept intact. This processing step generated three curved Gabor filter values for each image, enabling us to answer the question of whether a weighted combination of degrees of curvature could explain some of the brain activity.

Three curved Gabor filter values from each image were averaged across images to generate three curved Gabor filter values for each condition. The procedure was repeated for all six conditions, which generated 18 curvature values, with three for each condition.

The fMRI responses from five out of the six conditions were regressed with those curved Gabor filter values of the five conditions, which generated three regression coefficients and one intercept. Then the three curved Gabor filter values from the condition excluded from the regression were multiplied with the three regression coefficients, and added together with the intercept to generate a predicted response for the condition left out from the regression. By repeating the steps using the leave-one-out method, we generated six predicted responses.

The above steps were applied to the activity data for each animal individually. The mean predicted responses averaged across animals were correlated with the group averaged fMRI responses. To evaluate the statistical significance of the correlation, the same procedures were repeated again for each animal, except that the 18 curved Gabor filter values were randomly shuffled before generating the predicted response. Then, the mean predicted responses from the permutation test were correlated with the averaged fMRI response. This permutation test was repeated 1,000 times to determine the *P* value of the correlation.

ACKNOWLEDGMENTS. The study was supported by National Institute of Mental Health Intramural Research Program (X.Y., I.S.P., and L.G.U.) and National Institutes of Health Grant R01 EY017081 (to R.B.H.T.).

1. Hubel DH, Wiesel TN (1959) Receptive fields of single neurones in the cat's striate cortex. *J Physiol* 148:574–591.
2. Tanaka K (1996) Inferotemporal cortex and object vision. *Annu Rev Neurosci* 19:109–139.
3. Kourtzi Z, Connor CE (2011) Neural representations for object perception: Structure, category, and adaptive coding. *Annu Rev Neurosci* 34:45–67.
4. DiCarlo JJ, Zoccolan D, Rust NC (2012) How does the brain solve visual object recognition? *Neuron* 73(3):415–434.
5. Lehky SR, Sejnowski TJ (1988) Network model of shape-from-shading: Neural function arises from both receptive and projective fields. *Nature* 333(6172):452–454.
6. Gallant JL, Braun J, Van Essen DC (1993) Selectivity for polar, hyperbolic, and Cartesian gratings in macaque visual cortex. *Science* 259(5091):100–103.
7. Gallant JL, Connor CE, Rakshit S, Lewis JW, Van Essen DC (1996) Neural responses to polar, hyperbolic, and Cartesian gratings in area V4 of the macaque monkey. *J Neurophysiol* 76(4):2718–2739.
8. Pasupathy A, Connor CE (1999) Responses to contour features in macaque area V4. *J Neurophysiol* 82(5):2490–2502.
9. Pasupathy A, Connor CE (2001) Shape representation in area V4: Position-specific tuning for boundary conformation. *J Neurophysiol* 86(5):2505–2519.
10. Pasupathy A, Connor CE (2002) Population coding of shape in area V4. *Nat Neurosci* 5(12):1332–1338.
11. Kosslyn SM, Hamilton SE, Bernstein JH (1995) The perception of curvature can be selectively disrupted in prosopagnosia. *Brain Cogn* 27(1):36–58.
12. Tsao DY, Freiwald WA, Tootell RB, Livingstone MS (2006) A cortical region consisting entirely of face-selective cells. *Science* 311(5761):670–674.
13. Ohayon S, Freiwald WA, Tsao DY (2012) What makes a cell face selective? The importance of contrast. *Neuron* 74(3):567–581.
14. Wilkinson F, et al. (2000) An fMRI study of the selective activation of human extrastriate form vision areas by radial and concentric gratings. *Curr Biol* 10(22): 1455–1458.
15. Puce A, Allison T, Gore JC, McCarthy G (1995) Face-sensitive regions in human extrastriate cortex studied by functional MRI. *J Neurophysiol* 74(3):1192–1199.
16. Kanwisher N, McDermott J, Chun MM (1997) The fusiform face area: A module in human extrastriate cortex specialized for face perception. *J Neurosci* 17(11): 4302–4311.
17. Gattass R, Sousa APB, Gross CG (1988) Visuotopic organization and extent of V3 and V4 of the macaque. *J Neurosci* 8(6):1831–1845.
18. Freiwald WA, Tsao DY, Livingstone MS (2009) A face feature space in the macaque temporal lobe. *Nat Neurosci* 12(9):1187–1196.
19. Hadj-Bouziane F, Bell AH, Knusten TA, Ungerleider LG, Tootell RBH (2008) Perception of emotional expressions is independent of face selectivity in monkey inferior temporal cortex. *Proc Natl Acad Sci USA* 105(14):5591–5596.
20. Bell AH, Hadj-Bouziane F, Frihauf JB, Tootell RBH, Ungerleider LG (2009) Object representations in the temporal cortex of monkeys and humans as revealed by functional magnetic resonance imaging. *J Neurophysiol* 101(2):688–700.
21. Rajimehr R, Tootell RB (2009) Does retinotopy influence cortical folding in primate visual cortex? *J Neurosci* 29(36):11149–11152.
22. Sharpee TO, Kouh M, Reynolds JH (2013) Trade-off between curvature tuning and position invariance in visual area V4. *Proc Natl Acad Sci USA* 110(28):11618–11623.
23. Nandy AS, Sharpee TO, Reynolds JH, Mitchell JF (2013) The fine structure of shape tuning in area V4. *Neuron* 78(6):1102–1115.
24. Rousselet GA, Thorpe SJ, Fabre-Thorpe M (2004) How parallel is visual processing in the ventral pathway? *Trends Cogn Sci* 8(8):363–370.
25. Brincat SL, Connor CE (2004) Underlying principles of visual shape selectivity in posterior inferotemporal cortex. *Nat Neurosci* 7(8):880–886.
26. Tanaka K, Saito H, Fukada Y, Moriya M (1991) Coding visual images of objects in the inferotemporal cortex of the macaque monkey. *J Neurophysiol* 66(1):170–189.
27. Fujita I, Tanaka K, Ito M, Cheng K (1992) Columns for visual features of objects in monkey inferotemporal cortex. *Nature* 360(6402):343–346.
28. Talbot SA, Marshall WH (1941) Physiological studies on neural mechanisms of visual localization and discrimination. *Am J Ophthalmol* 24(11):1255–1264.
29. Daniel PM, Whitteridge D (1961) The representation of the visual field on the cerebral cortex in monkeys. *J Physiol* 159:203–221.
30. Tootell RB, Silverman MS, Switkes E, De Valois RL (1982) Deoxyglucose analysis of retinotopic organization in primate striate cortex. *Science* 218(4575):902–904.
31. Boussaoud D, Desimone R, Ungerleider LG (1991) Visual topography of area TEO in the macaque. *J Comp Neurol* 306(4):554–575.
32. Desimone R, Gross CG (1979) Visual areas in the temporal cortex of the macaque. *Brain Res* 178(2-3):363–380.
33. Nasr S, et al. (2011) Scene-selective cortical regions in human and nonhuman primates. *J Neurosci* 31(39):13771–13785.
34. Kornblith S, Cheng X, Ohayon S, Tsao DY (2013) A network for scene processing in the macaque temporal lobe. *Neuron* 79(4):766–781.
35. Epstein R, Kanwisher N (1998) A cortical representation of the local visual environment. *Nature* 392(6676):598–601.
36. Nasr S, Tootell RB (2012) A cardinal orientation bias in scene-selective visual cortex. *J Neurosci* 32(43):14921–14926.
37. Nasr S, Echavarria CE, Tootell RBH (2014) Thinking outside the box: Rectilinear shapes selectively activate scene-selective cortex. *J Neurosci* 34(20):6721–6735.
38. Rajimehr R, Devaney KJ, Bilenko NY, Young JC, Tootell RBH (2011) The "parahippocampal place area" responds preferentially to high spatial frequencies in humans and monkeys. *PLoS Biol* 9(4):e1000608.
39. Hubel DH, Wiesel TN (1970) Stereoscopic vision in macaque monkey. Cells sensitive to binocular depth in area 18 of the macaque monkey cortex. *Nature* 225(5227):41–42.

40. Tootell RBH, Hamilton SL, Silverman MS, Switkes E (1988) Functional anatomy of macaque striate cortex. I. Ocular dominance, binocular interactions, and baseline conditions. *J Neurosci* 8(5):1500–1530.
41. Hubel DH, Wiesel TN, Stryker MP (1978) Anatomical demonstration of orientation columns in macaque monkey. *J Comp Neurol* 177(3):361–380.
42. Livingstone MS, Hubel DH (1984) Anatomy and physiology of a color system in the primate visual cortex. *J Neurosci* 4(1):309–356.
43. Tootell RB, Hamilton SL (1989) Functional anatomy of the second visual area (V2) in the macaque. *J Neurosci* 9(8):2620–2644.
44. Petersen SE, Baker JF, Allman JM (1985) Direction-specific adaptation in area MT of the owl monkey. *Brain Res* 346(1):146–150.
45. Bell AH, et al. (2011) Relationship between functional magnetic resonance imaging-identified regions and neuronal category selectivity. *J Neurosci* 31(34):12229–12240.
46. Fize D, et al. (2003) The retinotopic organization of primate dorsal V4 and surrounding areas: A functional magnetic resonance imaging study in awake monkeys. *J Neurosci* 23(19):7395–7406.
47. Kolster H, et al. (2009) Visual field map clusters in macaque extrastriate visual cortex. *J Neurosci* 29(21):7031–7039.
48. Pfeuffer J, Merkle H, Beyerlein M, Steudel T, Logothetis NK (2004) Anatomical and functional MR imaging in the macaque monkey using a vertical large-bore 7 tesla setup. *Magn Reson Imaging* 22(10):1343–1359.
49. Ku SP, Tolias AS, Logothetis NK, Goense J (2011) fMRI of the face-processing network in the ventral temporal lobe of awake and anesthetized macaques. *Neuron* 70(2):352–362.
50. Ungerleider LG, Galkin TW, Desimone R, Gattass R (2008) Cortical connections of area V4 in the macaque. *Cereb Cortex* 18(3):477–499.
51. Hegdé J, Van Essen DC (2007) A comparative study of shape representation in macaque visual areas V2 and V4. *Cereb Cortex* 17(5):1100–1116.
52. Hikosaka K (1997) Responsiveness of neurons in the posterior inferotemporal cortex to visual patterns in the macaque monkey. *Behav Brain Res* 89(1-2):275–283.
53. Guilford JP (1929) Illusory movement from a rotating barber pole. *Am J Psychol* 41:686–687.
54. Moeller S, Freiwald WA, Tsao DY (2008) Patches with links: A unified system for processing faces in the macaque temporal lobe. *Science* 320(5881):1355–1359.
55. Freiwald WA, Tsao DY (2010) Functional compartmentalization and viewpoint generalization within the macaque face-processing system. *Science* 330(6005):845–851.
56. Kayaert G, Biederman I, Op de Beeck HP, Vogels R (2005) Tuning for shape dimensions in macaque inferior temporal cortex. *Eur J Neurosci* 22(1):212–224.
57. Kayaert G, Biederman I, Vogels R (2005) Representation of regular and irregular shapes in macaque inferotemporal cortex. *Cereb Cortex* 15(9):1308–1321.
58. Op de Beeck HP, Deutsch JA, Vanduffel W, Kanwisher NG, DiCarlo JJ (2008) A stable topography of selectivity for unfamiliar shape classes in monkey inferior temporal cortex. *Cereb Cortex* 18(7):1676–1694.
59. Issa EB, Papanastassiou AM, DiCarlo JJ (2013) Large-scale, high-resolution neurophysiological maps underlying FMRI of macaque temporal lobe. *J Neurosci* 33(38):15207–15219.
60. Tootell RB, Hadjikhani N (2001) Where is "dorsal V4" in human visual cortex? Retinotopic, topographic and functional evidence. *Cereb Cortex* 11(4):298–311.
61. Betts LR, Wilson HR (2010) Heterogeneous structure in face-selective human occipitotemporal cortex. *J Cogn Neurosci* 22(10):2276–2288.
62. Nichols DF, Betts LR, Wilson HR (2010) Decoding of faces and face components in face-sensitive human visual cortex. *Front Psychol* 1:28.
63. Gauthier I, Skudlarski P, Gore JC, Anderson AW (2000) Expertise for cars and birds recruits brain areas involved in face recognition. *Nat Neurosci* 3(2):191–197.
64. Biederman I (1987) Recognition-by-components: A theory of human image understanding. *Psychol Rev* 94(2):115–147.
65. Hoffman DD, Richards WA (1984) Parts of recognition. *Cognition* 18(1-3):65–96.
66. Riggs LA (1973) Curvature as a feature of pattern vision. *Science* 181(4104):1070–1072.
67. Treisman A, Gormican S (1988) Feature analysis in early vision: Evidence from search asymmetries. *Psychol Rev* 95(1):15–48.
68. Ito H (2012) Cortical shape adaptation transforms a circle into a hexagon: A novel afterimage illusion. *Psychol Sci* 23(2):126–132.
69. Vanduffel W, et al. (2001) Visual motion processing investigated using contrast agent-enhanced fMRI in awake behaving monkeys. *Neuron* 32(4):565–577.
70. Leite FP, et al. (2002) Repeated fMRI using iron oxide contrast agent in awake, behaving macaques at 3 tesla. *Neuroimage* 16(2):283–294.
71. Brainard DH (1997) The Psychophysics Toolbox. *Spat Vis* 10(4):433–436.
72. Pelli DG (1997) The VideoToolbox software for visual psychophysics: Transforming numbers into movies. *Spat Vis* 10(4):437–442.
73. Yue X, Cassidy BS, Devaney KJ, Holt DJ, Tootell RBH (2011) Lower-level stimulus features strongly influence responses in the fusiform face area. *Cereb Cortex* 21(1):35–47.
74. Friston KJ, et al. (1995) Statistical parametric maps in functional imaging: A general linear approach. *Hum Brain Mapp* 2:189–210.
75. Fischl B, Sereno MI, Dale AM (1999) Cortical surface-based analysis. II: Inflation, flattening, and a surface-based coordinate system. *Neuroimage* 9(2):195–207.
76. Sasaki Y, et al. (2006) The radial bias: A different slant on visual orientation sensitivity in human and nonhuman primates. *Neuron* 51(5):661–670.
77. Tootell RBH, Tsao D, Vanduffel W (2003) Neuroimaging weighs in: Humans meet macaques in "primate" visual cortex. *J Neurosci* 23(10):3981–3989.
78. Krüger N (2001) Learning object representations using a priori constraints within ORASSYLL. *Neural Comput* 13(2):389–410.